

AT2017gfo: AN ANISOTROPIC AND THREE-COMPONENT KILONOVA COUNTERPART OF GW170817

ALBINO PEREGO,^{1,2,3} DAVID RADICE,^{4,5} AND SEBASTIANO BERNUZZI^{3,1}

¹*Istituto Nazionale di Fisica Nucleare, Sezione Milano Bicocca, gruppo collegato di Parma, Parco Area delle Scienze 7/A, I-43124 Parma, Italia*

²*Dipartimento di Fisica, Università degli Studi di Milano Bicocca, Piazza della Scienza 3, 20126 Milano, Italia*

³*Dipartimento di Scienze Matematiche Fisiche ed Informatiche, Università di Parma, , Parco Area delle Scienze 7/A, I-43124 Parma, Italia*

⁴*Institute for Advanced Study, 1 Einstein Drive, Princeton, NJ 08540, USA*

⁵*Department of Astrophysical Sciences, Princeton University, 4 Ivy Lane, Princeton, NJ 08544, USA*

ABSTRACT

The detection of a kilo/macronova electromagnetic counterpart (AT2017gfo) of the first gravitational wave signal compatible with the merger of two neutron stars (GW170817) has confirmed the occurrence of r-process nucleosynthesis in this kind of events. The blue and red components of AT2017gfo have been interpreted as the signature of multi-component ejecta in the merger dynamics. However, the explanation of AT2017gfo in terms of the properties of the ejecta and of the ejection mechanisms is still incomplete. In this work, we analyse AT2017gfo with a new semi-analytic model of kilo/macronova inferred from general relativistic simulations of the merger and long-term numerical models of the merger aftermath. The model accounts for the anisotropic emission from the three known mass ejecta components: dynamic, winds and secular outflows from the disk. The early multi-band light-curves of AT2017gfo can only be explained by the presence of a relatively low opacity component of the ejecta at high latitudes. This points to the key role of weak interactions in setting the ejecta properties and determining the nucleosynthetic yields. Our model constrains also the total ejected mass associated to AT2017gfo to be between 0.042 and 0.077 M_{\odot} ; the observation angle of the source to be between $\pi/12$ and $7\pi/36$; and the mass of the disk to be $\gtrsim 0.08M_{\odot}$.

Keywords: stars: neutron — nuclear reactions, nucleosynthesis, abundances — infrared, ultraviolet:
individual AT2017gfo

1. INTRODUCTION

The discovery of the gravitational wave (GW) signal GW170817 by the LIGO and Virgo collaborations has marked the beginning of the multimessenger astronomy era (Abbott et al. 2017c; Abbott et al. 2017). GW170817 represents not only the first observed GW signal compatible with merging binary neutron stars (BNS), but also the first GW discovery followed by a cascade of electromagnetic (EM) signals recorded by telescopes in space and all over the world, across the entire EM spectrum (Abbott et al. 2017), from gamma-rays (Abbott et al. 2017b) to radio emission (Alexander et al. 2017).

As first pointed out by Lattimer & Schramm (1974), the ejection of neutron star matter from a compact merger is a favorable site for the production of the heaviest elements via the so-called r-process nucleosynthesis. The radioactive decay of the freshly synthesized neutron-rich r-process elements powers a transient called “kilonova” or “macronova” (MKN, Li & Paczyński 1998; Rosswog 2005; Metzger et al. 2010; Roberts et al. 2011; Kasen et al. 2013; Tanaka & Hotokezaka 2013; the term “macronova” initially referred to a transient powered by free-neutron and Nickel decay, Kulkarni 2005).

AT2017gfo has been interpreted as the MKN associated with GW170817. It peaked in less than one day after the merger in the optical and ultraviolet bands, before fading out rapidly (Nicholl et al. 2017). Meanwhile, the near infrared (IR) luminosity raised, reaching a maximum several days after the merger (Chornock et al. 2017). The former MKN peak is called the blue component (BC), while the latter the red component (RC). These two components could arise because of the strong dependence of the opacity of the material on the fraction of lanthanides and actinides. Material undergoing full r-process nucleosynthesis will produce substantial amount of lanthanides and actinides, so its presence can explain the RC (Kasen et al. 2013). On the other hand, the BC can be explained by ejecta that experienced only a partial r-process nucleosynthesis and is free from lanthanides and actinides (Martin et al. 2015). The presence of a BC might be also explained by other mechanisms, for example by the energy deposition of a relativistic jet in a cocoon of ejecta (Lazzati et al. 2017; Bromberg et al. 2017).

For a radioactively powered MKN, the occurrence of a RC, of a BC or of both depends on the physical and geometrical properties of the ejecta. Matter from a BNS merger is expected to be expelled over the whole solid angle, but not necessarily to be isotropic. Moreover, several ejection mechanisms play a significant role during the merger, having a direct imprint on the ejecta properties. On the timescale of a few

ms, tidal interactions and shocks drive the ejection of the dynamic ejecta. Weak interactions can potentially alter its initial neutron-richness (Sekiguchi et al. 2015; Foucart et al. 2016; Radice et al. 2016; Bovard et al. 2017). However, equatorial ejecta seems to stay neutron-rich enough to produce the full r-process nucleosynthesis (Martin et al. 2017). If the merger does not lead to the prompt collapse of the central massive neutron star (MNS), neutrino-matter interactions and magnetic processes produce wind outflows (Perego et al. 2014). The larger timescale (10s ms) and the polar character of this ejection allow matter to increase its electron fraction (Y_e), preventing the nucleosynthesis of the heaviest r-process elements. If during the merger a disk has formed, on its longer lifetime (100s ms) the spreading due to viscous processes and the subsequent nuclear recombination unbind a fraction of the disk (Metzger et al. 2009; Fernández & Metzger 2013; Metzger & Fernández 2014; Just et al. 2015). Numerical studies of this secular ejecta revealed rather homogeneous distributions of the ejecta properties, emitted at all latitudes and leading to full r-process nucleosynthesis (Wu et al. 2016; Siegel & Metzger 2017).

Recent work on the interpretation of AT2017gfo has revealed that a single component model for the MKN is inadequate to reproduce the observed features in all bands. Two or even three component models are necessary (Cowperthwaite et al. 2017; Tanvir et al. 2017; Tanaka et al. 2017). In all of them a fast, low opacity ejection is responsible for the BC, while a slower, more opaque ejection accounts for the RC (Abbott et al. 2017a). The most sophisticated MKN models are based on radiative transport schemes, nonetheless most of them assume a spherical geometry.

In this work, we show that the BC and the RC of the MKN in all relevant bands can be explained by an anisotropic model with multi-component ejecta. Our model builds on general-relativistic merger simulations and aftermath simulations of neutrino and viscosity-driven ejecta, and it directly relates the geometry and the physical ejection mechanisms to the light curves. By reproducing the observed light curves we confirm that the ejecta properties are highly anisotropic and inhomogeneous. Moreover, we constrain some of the properties of the merging system and prove the central role of weak interaction in BNS mergers.

2. ANISOTROPIC THREE-COMPONENT SEMI-ANALYTICAL MKN MODEL

We propose a semi-analytical MKN model with dependence on the polar angle and composed of three ejecta components: the dynamic, the wind and the secular

ejecta. The ejecta propagation and the electromagnetic radiation are computed by an extension of the model presented in Grossman et al. (2014) and Martin et al. (2015).

2.1. Ejecta components

Dynamic.—The geometry and composition of the dynamic ejecta is inferred by general-relativistic hydrodynamical (GRHD) simulations of Radice et al. in prep. (2017). Figure 1 displays the angular distributions of the mass and Y_e for an exemplary case. The presence of shocks and intense neutrino irradiation increases Y_e above 0.25 close to the polar axis while the electron fraction stays below 0.25 across the equatorial plane. The crucial impact of neutrino absorption is visible by comparing simulations with and without neutrino heating. The ejection happens at all latitudes, but predominantly along the equatorial plane. Once neutrino heating is taken into account, the angular distribution is well approximated by $F(\theta) = \sin^2 \theta$. We remark that, according to our simulations, the overall geometry and composition of the outflow are insensitive to the nuclear equation of state (EOS) and the binary parameters, at least up to the mass ratios we have considered ($q \gtrsim 0.85$). On the other hand, the total dynamic ejecta mass ranges from $\sim 10^{-4} M_\odot$ to $\sim 10^{-2} M_\odot$. For this reason, only the formers are used to inform our MKN model. The ejecta velocity is mildly relativistic, $v_d \lesssim 0.3c$. If the merger does not lead to the prompt collapse of the massive neutron star (MNS) to a black hole (BH), tidal torques and mass ejection episodes from the rotating MNS produce a disk, with a mass $10^{-2} M_\odot \lesssim M_{\text{disk}} \lesssim 10^{-1} M_\odot$.

Wind.—The wind geometry is inferred from merger aftermath simulations of Martin et al. (2015). The ejection mechanisms favor polar emission with a rather uniform distribution in mass ($F(\theta) \approx \text{const}$ for $\theta \lesssim \theta_w \approx \pi/3$) and velocity $v_w \lesssim 0.08c$. The ejected mass is a fraction of the disk mass, $m_{\text{ej},w} = \xi_w M_{\text{disk}}$ with $\xi_w \sim 0.05$. Neutrino irradiation has enough time to unbind matter from the disk and to increase Y_e above 0.25, preventing full r-process nucleosynthesis.

Secular.—The properties of secular ejecta are inspired by simulations of disks around a MNS or a BH (Wu et al. 2016; Lippuner et al. 2017; Siegel & Metzger 2017). This ejecta is expected to unbind a significant fraction of the disk $m_{\text{ej},v} = \xi_v M_{\text{disk}}$, where $\xi_v \lesssim 0.3$, with a rather uniform velocity distribution and $v_s \lesssim 0.05c$. We consider an equatorial-dominated flow, $F_s(\theta) = \sin^2 \theta$ and two cases for the Y_e distribution: $0.1 \lesssim Y_e(\theta) \lesssim 0.4$, for a MNS collapsing to a BH on a timescale shorter than

the disk lifetime (Siegel & Metzger 2017), and $0.25 \lesssim Y_e(\theta) \lesssim 0.5$ for an extremely long-lived MNS (Lippuner et al. 2017).

2.2. Ejecta expansion and radiative model

We assume the ejecta to be axisymmetric around the rotational axis of the remnant and symmetric with respect to the equatorial plane. The polar angle θ is discretized in 12, equally spaced bins. Each mass ejection is characterized by a) its mass, m_{ej} , b) its rms radial speed, v_{rms} , c) its opacity, κ ; alongside with their angular distributions. For the mass, we introduce a distribution $F(\theta)$ such that:

$$m_{\text{ej}} = \sum_{k=1,12} m_{\text{ej},k} = \sum_{k=1,12} 2\pi \int_{\theta_k - \Delta\theta/2}^{\theta_k + \Delta\theta/2} F(\theta) \sin \theta d\theta. \quad (1)$$

For v_{rms} , we assume $v_{\text{rms}}(\theta) = \text{const}$. We assign the opacity according to the value of Y_e for the bulk of the ejecta. If Y_e is such that $Y_e(\theta) \gtrsim 0.25$ for $\theta < \theta_{\text{lim}}$ and $Y_e(\theta) \lesssim 0.25$ for $\theta > \theta_{\text{lim}}$, then we set $\kappa(\theta > \theta_{\text{lim}}) = \kappa_{\text{max}} \gtrsim 10 \text{ cm}^2 \text{ g}^{-1}$ and $\kappa(\theta < \theta_{\text{lim}}) = \kappa_{\text{min}} \lesssim 1 \text{ cm}^2 \text{ g}^{-1}$. Otherwise, if for all θ angles Y_e has a broad distribution across 0.25, we assign $\kappa(\theta) = \kappa_{\text{avg}}$ with $\kappa_{\text{min}} \lesssim \kappa_{\text{avg}} \lesssim \kappa_{\text{max}}$.

Within each bin, we run the radial model of Grossman et al. (2014) for each ejecta component. We further assume that the energy emitted by the two innermost photospheres is deposited at the basis of the outermost shell or inside its radiating envelope, and gets quickly reprocessed and emitted by the outermost photosphere. The energy that powers the MKN is expressed as $Q = \Delta M_{\text{env}} \epsilon_{\text{nuc}}$ where ΔM_{env} is the mass of the radiating shell enclosed between the diffusion and the free streaming photosphere, R_{ph} . The nuclear heating rate, ϵ_{nuc} , is approximated by an analytic fitting formula, derived from detailed nucleosynthesis calculations (Korobkin et al. 2012):

$$\epsilon_{\text{nuc}}(t) = \epsilon_0 \epsilon_{Y_e}(t) \left(\frac{\epsilon_{\text{th}}}{0.5} \right) \left[\frac{1}{2} - \frac{1}{\pi} \arctan \left(\frac{t - t_0}{\sigma} \right) \right], \quad (2)$$

where $\sigma = 0.11 \text{ s}$, $t_0 = 1.3 \text{ s}$, and ϵ_{th} is the thermalization efficiency (Table 1 and Equation (36) of Barnes et al. (2016)). Korobkin et al. (2012) found $\epsilon_0 = 1.2 \times 10^{18} \text{ erg g}^{-1} \text{ s}^{-1}$ using the finite range droplet model (FRDM, Möller et al. 1995). Due to the large uncertainties in the nuclear mass and decay models, we consider ϵ_0 as a free parameter with $2 \times 10^{18} \text{ erg s}^{-1} \text{ g}^{-1} \lesssim \epsilon_0 \lesssim 2 \times 10^{19} \text{ erg g}^{-1} \text{ s}^{-1}$ (e.g. Mendoza-Temis et al. 2015; Rosswog et al. 2017). Detailed calculations of neutrino-driven wind nucleosynthesis revealed the dominant presence of first r-process peak nuclei with a decay

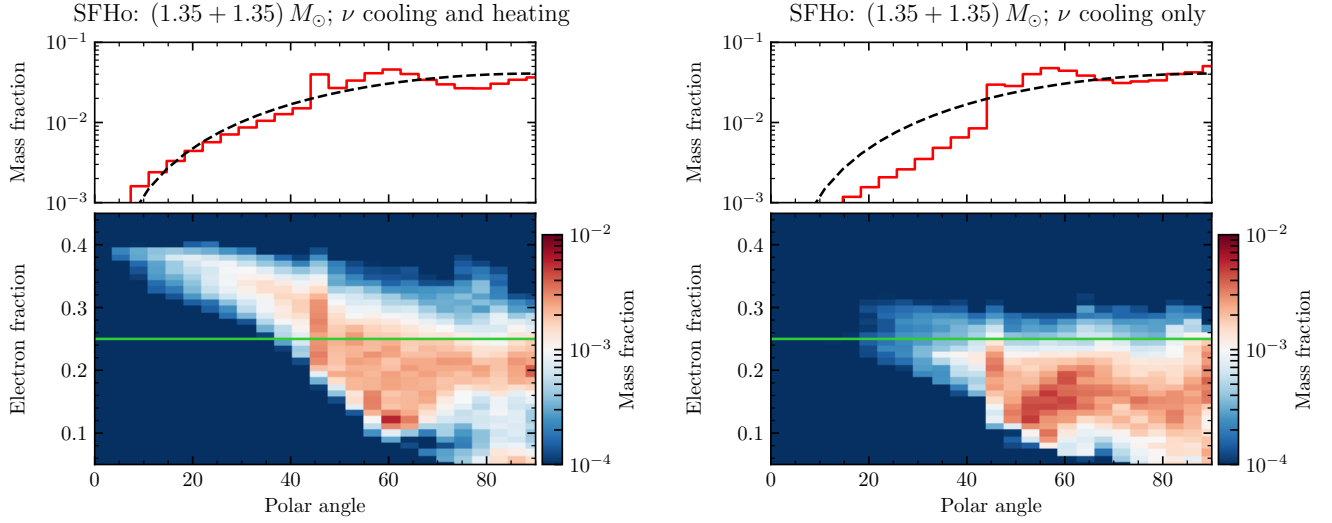


Figure 1. Angular profile and composition of dynamic ejecta computed from GRHD BNS merger simulations of an equal-mass binary of $2.7M_{\odot}$ with SFHo EOS (Radice et al. in prep. 2017). Left: Simulation with neutrino cooling and heating. Right: Simulation with neutrino cooling only. The small bump in the ejecta distribution at 45° is an artifact imprinted by our Cartesian grid, which preferentially channels flow along its symmetry directions (Radice et al. 2016). The angular profile of the simulation including neutrino cooling and heating is well described by $\sin^2 \theta$.

Table 1. Left: Parameters for the exploration of the model. Right: Parameters of the best fits to AT2017gfo.

	Parameter range	BF	BF _c	BF _{c,ε}
χ^2	-	759	1263	1448
$M_{\text{disk}} [M_{\odot}]$	{0.01; 0.08; 0.1; 0.12; 0.15; 0.2}	0.08	0.1	0.12
$m_{\text{ej,d}} [10^{-2}M_{\odot}]$	{0.05; 0.5; 1.0; 2.0; 5.0}	1.0	0.5	0.5
ξ_w	{0.001; 0.05; 0.1; 0.15; 0.2}	0.001	0.15	0.2
ξ_s	{0.001; 0.1; 0.2; 0.3; 0.4}	0.4	0.2	0.4
$\theta_{\text{lim,d}}$	{ $\pi/6$; $\pi/4$ }	$\pi/4$	$\pi/6$	$\pi/6$
$\theta_{\text{lim,w}}$	{ $\pi/6$; $\pi/4$ }	$\pi/6$	$\pi/6$	$\pi/4$
$v_{\text{rms,d}} [c]$	{0.1; 0.13; 0.17; 0.2; 0.23}	0.2	0.23	0.2
$v_{\text{rms,w}} [c]$	{0.033; 0.05; 0.067}	0.067	0.067	0.067
$v_{\text{rms,s}} [c]$	{0.017; 0.027; 0.033; 0.04}	0.027	0.04	0.04
$\kappa_d [\text{cm g}^{-1}]$	{(0.5, 30); (1, 30)}	(1,30)	(1,30)	(1,30)
$\kappa_w [\text{cm g}^{-1}]$	{(0.5, 5); (0.1, 1)}	(0.1,1)	(0.5,5)	(0.5,5)
$\kappa_s [\text{cm g}^{-1}]$	{1; 5; 10; 30}	1	5	5
θ_{obs}	$n \pi/36$ for $n = 0 \dots 11$	$\pi/12$	$5\pi/36$	$7\pi/36$
$\epsilon_0 [10^{18} \text{erg g}^{-1} \text{s}^{-1}]$	{2; 6; 12; 16; 20}	16	20	12

NOTE—BF: best fit parameter set. BF_c: best fit parameter set once $M_{\text{disk}} \leq 0.12 M_{\odot}$, $m_{\text{ej,d}} \leq 0.01 M_{\odot}$ and $\kappa_s \geq 5.0 \text{ cm}^2 \text{g}^{-1}$ are imposed. BF_{c,ε}: best fit when $\epsilon_0 \leq 12 \times 10^{18} \text{erg g}^{-1} \text{s}^{-1}$ is also imposed.

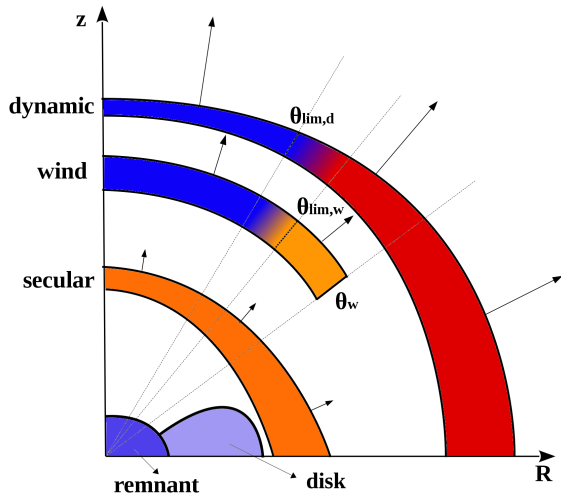


Figure 2. Graphical sketch of the three ejecta components radially expanding from the remnant. Different colors correspond to different matter opacity: high (red), intermediate (orange), low (blue).

half-life of a few hours (Table 1, Martin et al. 2015). The associated specific heating rate showed that ϵ_{nuc} can significantly differ from the one of extremely neutron rich ejecta for $Y_e \gtrsim 0.25$ (Figure 13, Martin et al. 2015). Thus, we have introduced the factor ϵ_{Y_e} such that $\epsilon_{Y_e}(t) = \epsilon_{\text{min}} + \epsilon_{\text{max}} \{1 + \exp[4(t/t_\epsilon - 1)]\}^{-1}$, with $t_\epsilon = 1$ d, $\epsilon_{\text{min}} = 0.5$ and $\epsilon_{\text{max}} = 2.5$ if $Y_e \gtrsim 0.25$, and $\epsilon_{Y_e}(t) = 1$ otherwise.

We locate an observer at a distance $d \gg R_{\text{ph}}$, with a viewing angle θ_{obs} measured from the symmetry axis. From the analysis of GW170817, we set $d = 40$ Mpc and $\theta_{\text{obs}} < \pi 11/36$ (Abbott et al. 2017c). The observed spectral flux is computed as a superposition of Planckian distributions weighted by the projection of the emitting surface along the view line (Equations 4 and 5 in Martin et al. 2015).

Figure 2 provides a sketch of the system geometry and of the opacity properties of the ejecta. The three-component anisotropic matter ejection produces a rich light curve with peaks proceeding from the ultraviolet to the near-IR on a timescale of a few days. The presence of a low opacity ejecta close to the polar axis produces a BC with a peak within the first day after the merger. The RC of the emission is produced by all ejecta, with a dominant contribution from the more opaque dynamic ejecta and the more abundant secular ejecta. The wind contributes to both components, sustaining the BC for a timescale ~ 1 d and, at the same time, powering the first phase of the RC.

3. RESULTS

We compare the light curves of AT2017gfo in the visible and near-IR with predictions of our model. The observed apparent magnitudes are taken from Pian et al. (2017) for the photometric filters B , V , R , r , g , i , and z ; and from Tanvir et al. (2017) for the filters K_s and J .

The parameter space of our model is explored by constructing a discrete grid for each parameter as indicated in Table 1. The agreement between a model (specified by a set of parameters) and the data is quantified using the function,

$$\chi^2 = \sum_{n=1}^{N_{\text{fts}}} \left(\sum_{k=1}^{N_{\text{pts}}(n)} \left(\frac{m_{k,n}^{\text{obs}} - m_{k,n}^{\text{mod}}}{\sigma_{k,n}^{\text{obs}}} \right)^2 \right), \quad (3)$$

where $N_{\text{fts}} = 9$ is the number of filters used in the comparison, $N_{\text{pts}}(n)$ the number of points in each light curve, $m_{k,n}^{\text{mod}}$ the apparent magnitudes given by our model and $m_{k,n}^{\text{obs}} \pm \sigma_{k,n}^{\text{obs}}$ the observed apparent magnitudes with their uncertainties. Three physically motivated best fit models are discussed in the following.

We first assume no constraints on the parameters within our grid. Among all the models, we found a minimum for $\chi^2 = 759$. The corresponding parameter set is reported as BF in Table 1 and the light curves are represented in Figure 3 (solid lines). This model is characterized by a subdominant wind component and by a secular ejecta whose opacity is such that $\kappa_s \ll \kappa_{\text{d,max}}$, but $\kappa_s \sim \kappa_{\text{w,max}}$. Thus, our three-component model has reduced to an effective two-component model in which the formation of a significant fraction of the heaviest r-process elements is not expected inside the secular ejecta. The lower κ_s is compensated by a slower expansion, to reproduce the features of the RC.

Due to the peculiar conditions required to underproduce lanthanides and actinides in the secular ejecta (i.e., an extremely long-lived MNS, Lippuner et al. 2017), we repeat the analysis by imposing the production of a significant amount of heavy r-process elements in this ejecta, i.e. assuming $0.1 \lesssim Y_{e,s} \lesssim 0.4$ and $\kappa_s \geq 5.0 \text{ cm}^2 \text{ g}^{-1}$. This constraint alone would result in models with $M_{\text{disk}} \geq 0.2 M_\odot$ and $m_{\text{ej,d}} \geq 2 \times 10^{-2} M_\odot$, in tension with results from GRHD simulations. Hence, we impose two more constraints: $m_{\text{ej,dyn}} \leq 0.01 M_\odot$ and $M_{\text{disk}} \leq 0.12 M_\odot$. Under these additional hypothesis, we obtain a new parameter set (BF_c in Table 1) whose fit quality has decreased compared with BF ($\chi^2 = 1263$). The dashed lines in Figure 3 show the corresponding light curves. In this model, the wind component is now present and well distinct from the secular ejecta. Moreover, the opacity for the polar dynamic and polar wind ejecta are comparable. The amount of wind ejecta (rel-

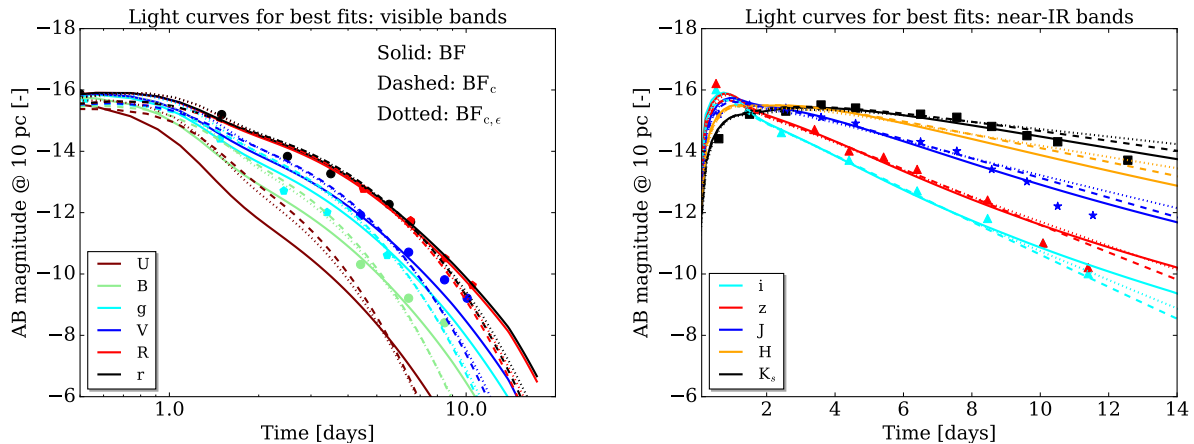


Figure 3. Visible (left) and near-IR (right) light curves obtained for the best fit models reported in Table 1: BF (solid), BF_c (dashed), $BF_{c,\epsilon}$ (dotted).

ative to the disk mass) obtained for BF_c is significantly above the results reported in Martin et al. (2015) for pure neutrino-driven winds, suggesting a non-negligible role of magnetically-driven winds, while the amount of secular ejecta is in agreement with the results reported in Just et al. (2015), Fernández & Metzger (2013) and Siegel & Metzger (2017). In Figure 4, we explore the sensitivity of our model by varying independently a single parameter with respect to the BF_c set. The different panels show that the most relevant light curve features (e.g., peak strength and time, decline behavior) are primarily influenced by the total amount of emitting matter and by the time when matter becomes transparent.

For both BF and BF_c , the observed brightness requires a heating rate larger than the heating rate predicted by theoretically nuclear mass models, even within presently nuclear uncertainties (e.g. Rosswog et al. 2017). To explore this uncertainty, we search for the minimum χ^2 imposing an additional constraint on the nuclear heating rate, $\epsilon_0 \leq 1.2 \times 10^{19} \text{ erg g}^{-1} \text{ s}^{-1}$, still compatible with nuclear mass models (Duflo & Zuker 1995). The result is reported in Table 1 as $BF_{c,\epsilon}$ and in Figure 3 as dotted lines. The agreement with the observations further reduces and χ^2 increases by $\sim 15\%$. Most of the model parameters remain the same as for BF_c , while the reduced heating rate is compensated by an increase in the fraction of the disk ejected as wind or secular ejecta.

For all best-fit MKN models, the emission is produced by a substantial amount of ejecta: $m_{\text{ej}} \equiv (m_{\text{ej,d}} + m_{\text{ej,w}} + m_{\text{ej,s}}) = 0.0421, 0.04 M_\odot$, and $0.077 M_\odot$ for the BF, BF_c and $BF_{c,\epsilon}$, respectively. Our models favor a viewing angle $\pi/12 \leq \theta_{\text{obs}} \leq 7\pi/36$, with the lower bound (more consistent with GW170917) characterized by the presence of a smaller amount of mass ejected along the po-

lar direction. Variations of $\theta_{\text{lim,d(w)}}$ between $\pi/6$ and $\pi/4$ have a minor impact on our results, but more collimated wind outflows are more compatible with smaller θ_{obs} . Finally, the presence of a larger nuclear heating rate for the high- Y_e , polar ejecta at $t \lesssim t_\epsilon$ increases the light curves by half a magnitude during the first day. Thus, this correction is potentially relevant to explain the early behavior of the UV and visible light curves of a MKN.

4. CONCLUSION

In this *Letter*, we have interpreted AT2017gfo, the EM counterpart of GW170817, as the MKN emission produced by a multi-component and anisotropic distribution of the ejecta from a BNS merger.

The emission brightness requires a high nuclear heating rate in combination with an ejected mass in excess of $0.04 M_\odot$. A heating rate compatible with present nuclear uncertainties implies an even larger mass ejection, $0.077 M_\odot$. The amount of dynamic ejecta predicted by our models ($\sim 0.005 - 0.01 M_\odot$) is consistent (within present uncertainties) with typical values provided by GRHD simulations. Secular and wind ejecta play a central role and demand the presence of a disk with $M_{\text{disk}} \gtrsim 0.08 M_\odot$. The formation of such disks, compatible with numerical results, excludes that the merger outcome is a prompt collapse to a BH.

The presence of a BC in the MKN light curve is a signature of fast expanding, low opacity ejecta close to the polar region. However, reproducing its properties in combination with the ones of the RC requires the presence of matter with an opacity lower than $10 \text{ cm}^2 \text{ g}^{-1}$ and a more isotropic distribution, in addition to very opaque ejecta expected from the equatorial dynamic ejecta. These results indicate that weak processes are

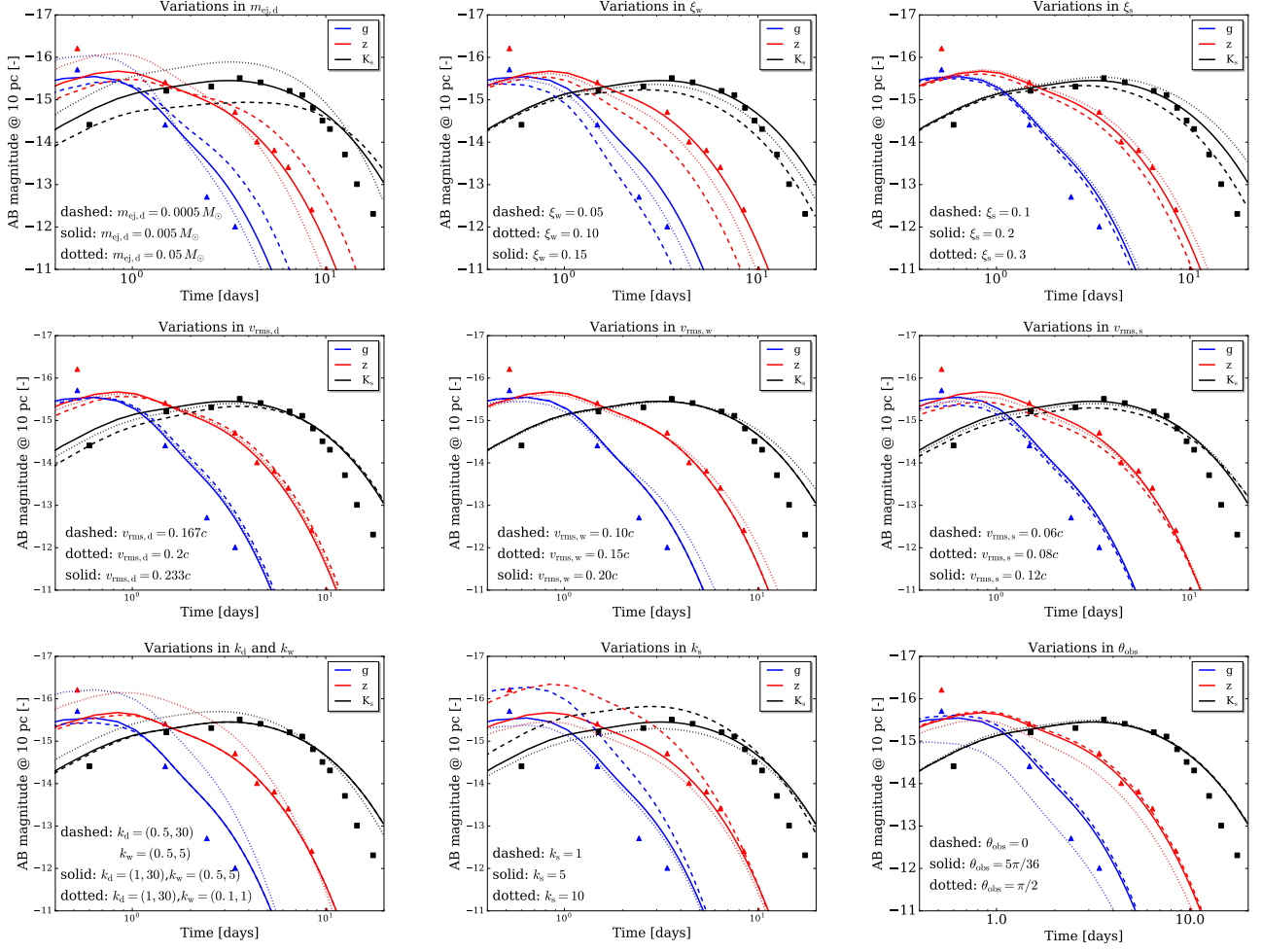


Figure 4. Light curves for the three filters g , z , K_s for several models obtained varying independently one parameter (dashed and dotted) with respect to the BF_c model (solid).

key to set the properties of a fraction of the ejecta and have a direct impact on the EM counterpart of BNS mergers.

The ratio between the magnitudes of the BC and RC also constrains the observer viewing angle to be $\pi/12 \lesssim \theta_{\text{obs}} \lesssim 7\pi/36$. This interval is fully consistent with the broader limit inferred from the GW signal alone ($\theta_{\text{obs}} \lesssim 11\pi/36$), while the limit including the information about the host galaxy distance (NGC4993, $\theta_{\text{obs}} \lesssim 7\pi/45$) is more consistent with an observer location at $\pi/12 \lesssim \theta_{\text{obs}} \lesssim 5\pi/36$.

The observed light curve of AT2017gfo is compatible both with a (effective) two- and a three-component ejecta model. The presence of a very long-lived MNS, necessary to explain the Y_e distribution required by the two-component model, implies a very efficient mechanism to prevent angular momentum redistribution and the subsequent collapse of the MNS (in particular for soft nuclear EOS). The three-component models require a reduced amount of dynamic ejecta, in association

with larger viewing angles (but still compatible with GW170817 constraints). The presence of a massive disk and of a wind component still demands a MNS phase, but for a timescale shorter than the disk lifetime.

In our analysis, we did not consider the possible presence of a small amount ($\sim 10^{-4} M_\odot$) of free-neutron ejecta (Bauswein et al. 2013), which could contribute to the UV/visible emission a few hours after the merger (Metzger et al. 2015). We anticipate that the inferred amount of polar outflow would decrease in the presence of this neutron skin, and we postpone its detailed study to a future work.

According to our models, the disk ejecta expands significantly slower than the dynamic ejecta. Its nucleosynthesis yields have more chances not to escape from the galaxy and to contribute to its metal enrichment. This could help explaining metal abundances in dwarf galaxies (Ji et al. 2016).

The discovery of AT2017gfo has represented a milestone in modern astrophysics. Our work indicate that

further analysis of such event will require including the influence of geometry, a detailed modeling of weak interactions in the merger aftermath (possibly accounting for neutrino oscillations, [Zhu et al. 2016](#)), and sophisticated GRHD models of BNS mergers that include viscosity effects and winds ([Shibata & Kiuchi 2017](#); [Radice 2017](#)).

The authors thank O. Salafia, T. Venumadhav, and M. Zaldarriaga for useful discussions. A.P. and D.R. acknowledge support from the Institute for Nuclear Theory (17-2b program). S.B. acknowledges support by the

EU H2020 under ERC Starting Grant, no. BinGraSp-714626. D.R. acknowledges support from a Frank and Peggy Taplin Membership at the Institute for Advanced Study and the Max-Planck/Princeton Center (MPPC) for Plasma Physics (NSF PHY-1523261) Computations were performed the on supercomputers Marconi/CINECA (PRACE proposal 2016153522), Stampede, Comet, and Bridges (NSF XSEDE allocation TG-PHY160025), on NSF/NCSA Blue Waters (NSF PRAC ACI-1440083), and PizDaint/CSCS (ID 667).

REFERENCES

- Abbott, B. P., et al. 2017a, Submitted to: *Astrophys. J.*, [arXiv:1710.05836 \[astro-ph.HE\]](#)
- . 2017b, *Astrophys. J.*, **848**, L13
- . 2017c, *Phys. Rev. Lett.*, **119**, 161101
- Abbott, B. P., Abbott, R., Abbott, T. D., et al. 2017, *ApJL*, **848**, L12
- Alexander, K. D., et al. 2017, *Astrophys. J.*, **848**, L21
- Barnes, J., Kasen, D., Wu, M.-R., & Martínez-Pinedo, G. 2016, *Astrophys. J.*, **829**, 110
- Bauswein, A., Goriely, S., & Janka, H.-T. 2013, *ApJ*, **773**, 78
- Bovard, L., Martin, D., Guercilena, F., et al. 2017, ArXiv e-prints, [arXiv:1709.09630 \[gr-qc\]](#)
- Bromberg, O., Tchekhovskoy, A., Gottlieb, O., Nakar, E., & Piran, T. 2017, [arXiv:1710.05897 \[astro-ph.HE\]](#)
- Chornock, R., et al. 2017, [arXiv:1710.05454 \[astro-ph.HE\]](#)
- Cowperthwaite, P. S., et al. 2017, *Astrophys. J.*, **848**, L17
- Duflo, J., & Zuker, A. P. 1995, *PhRvC*, **52**, R23
- Fernández, R., & Metzger, B. D. 2013, *MNRAS*, **435**, 502
- Foucart, F., Haas, R., Duez, M. D., et al. 2016, *PhRvD*, **93**, 044019
- Grossman, D., Korobkin, O., Rosswog, S., & Piran, T. 2014, *MNRAS*, **439**, 757
- Ji, A. P., Frebel, A., Chiti, A., & Simon, J. D. 2016, *Nature*, **531**, 610
- Just, O., Bauswein, A., Pulpillo, R. A., Goriely, S., & Janka, H.-T. 2015, *MNRAS*, **448**, 541
- Kasen, D., Badnell, N. R., & Barnes, J. 2013, *ApJ*, **774**, 25
- Korobkin, O., Rosswog, S., Arcones, A., & Winteler, C. 2012, *MNRAS*, **426**, 1940
- Kulkarni, S. R. 2005, ArXiv Astrophysics e-prints, [astro-ph/0510256](#)
- Lattimer, J. M., & Schramm, D. N. 1974, *ApJL*, **192**, L145
- Lazzati, D., Deich, A., Morsony, B. J., & Workman, J. C. 2017, *MNRAS*, **471**, 1652
- Li, L.-X., & Paczyński, B. 1998, *ApJL*, **507**, L59
- Lippuner, J., Fernández, R., Roberts, L. F., et al. 2017, *MNRAS*, **472**, 904
- Martin, D., Perego, A., Arcones, A., et al. 2015, *ApJ*, **813**, 2
- Martin, D., Perego, A., Kastaun, W., & Arcones, A. 2017, ArXiv e-prints, [arXiv:1710.04900 \[astro-ph.HE\]](#)
- Mendoza-Temis, J. d. J., Wu, M.-R., Langanke, K., et al. 2015, *PhRvC*, **92**, 055805
- Metzger, B. D., Arcones, A., Quataert, E., & Martínez-Pinedo, G. 2010, *MNRAS*, **402**, 2771
- Metzger, B. D., Bauswein, A., Goriely, S., & Kasen, D. 2015, *MNRAS*, **446**, 1115
- Metzger, B. D., & Fernández, R. 2014, *MNRAS*, **441**, 3444
- Metzger, B. D., Piro, A. L., & Quataert, E. 2009, *MNRAS*, **396**, 304
- Möller, P., Nix, J. R., Myers, W. D., & Swiatecki, W. J. 1995, *At. Data Nucl. Data Tables*, **59**, 185
- Nicholl, M., et al. 2017, *Astrophys. J.*, **848**, L18
- Perego, A., Rosswog, S., Cabezón, R. M., et al. 2014, *MNRAS*, **443**, 3134
- Pian, E., et al. 2017, *Nature*, [arXiv:1710.05858 \[astro-ph.HE\]](#)
- Radice, D. 2017, *ApJL*, **838**, L2
- Radice, D., Galeazzi, F., Lippuner, J., et al. 2016, *MNRAS*, **460**, 3255
- Roberts, L. F., Kasen, D., Lee, W. H., & Ramirez-Ruiz, E. 2011, *ApJL*, **736**, L21
- Rosswog, S. 2005, *ApJ*, **634**, 1202
- Rosswog, S., Feindt, U., Korobkin, O., et al. 2017, *Classical and Quantum Gravity*, **34**, 104001
- Sekiguchi, Y., Kiuchi, K., Kyutoku, K., & Shibata, M. 2015, *PhRvD*, **91**, 064059
- Shibata, M., & Kiuchi, K. 2017, *PhRvD*, **95**, 123003
- Siegel, D. M., & Metzger, B. D. 2017, ArXiv e-prints, [arXiv:1705.05473 \[astro-ph.HE\]](#)
- Tanaka, M., & Hotokezaka, K. 2013, *ApJ*, **775**, 113
- Tanaka, M., et al. 2017, *Publ. Astron. Soc. Jap.*, [arXiv:1710.05850 \[astro-ph.HE\]](#)

Tanvir, N. R., et al. 2017, *Astrophys. J.*, 848, L27
Wu, M.-R., Fernández, R., Martínez-Pinedo, G., &
Metzger, B. D. 2016, *MNRAS*, 463, 2323

Zhu, Y. L., Perego, A., & McLaughlin, G. C. 2016, *PhRvD*,
94, 105006